2011

Blind Yield Detection in Steel Structure for Automatic Nondestructive Testing Using Ultrasonic Sensors

Hongting Zhang
Louisiana State University and Agricultural and Mechanical College

BLIND YIELD DETECTION IN STEEL STRUCTURE FOR AUTOMATIC NONDESTRUCTIVE TESTING USING ULTRASONIC SENSORS

A Thesis
Submitted to the Graduate Faculty of the
Louisiana State University and
Agricultural and Mechanical College
in partial fulfillment of the
requirements for the degree of
Master of Science in Electrical Engineering

in

The Department of
Electrical and Computer Engineering

by
Hongting Zhang
B.S., Harbin Institute of Technology, 2009
December, 2011

To my parents

ACKNOWLEDGEMENTS

First, I would like to express my sincere gratitude to my thesis supervisor, Dr. Hsiao-Chun Wu, for his persistent guidance throughout my graduate study at Louisiana State University (LSU). His knowledge, inspiration, and expertise in this field really navigate my thesis work through to the destination. Without his encouragement, this thesis would never have been completed.

I would also like to convey my gratefulness to my thesis committee members, Dr. Xue-Bin Liang and Dr. Xin Li. They have been very supportive and gave me precious advices on this thesis.

Meanwhile, I would like to thank my beloved and devoted family, who have been backing me without any hesitation for all years, especially my dear husband. I would never have achieved my dreams without their selfless and loyal support.

Of course, I owe a lot of gratitude to my former and current labmates at LSU. Many thanks thus go to Dr. Kun Yan and Dr. Lu Lu, for their sharing invaluable information and knowledge with me all the time.

Last but not least, I greatly thank all my friends, for all your friendship and enrichment in my life.

TABLE OF CONTENTS

LIST OF TABLES

LIST OF FIGURES

ABSTRACT

Detection of yield zones using nondestructive testing (NDT) technology for assessing the structural integrity of the existing steel buildings/bridges is extremely important. The average energy over the "effective echoes" (in "good" signal quality) is a robust feature for the yield detection in steel structures. Nevertheless, this average-energy feature extraction requires rigorous manual data-acquisition and human operation. Therefore, in this thesis, we make the first-ever attempt to design a *totally-blind* and *automatic* steel-structure yield-detection mechanism, which requires neither the *a priori* information about the signal nor the human effort in calibration, operation, or data analysis. This new scheme is built upon a robust preprocessor, which involves both *blind-signature-signal-extraction* and *zero-crossing-rate thresholding*, to identify the starting and terminal time points of each ultrasonic echo. Thus, the new computer-aided system can easily estimate the signal-to-noise ratios and automatically extract the effective echoes to calculate the corresponding average energy. The performance reflected by the receiver-operating characteristic (ROC) curves of the proposed method is very close to that of the conventional human-operating technique. Hence one may save much human effort in the sacrifice of very little detection accuracy by using our proposed new system.

1. INTRODUCTION

The motivation, potential applications, and scope of this thesis will be introduced in the following sections.

1.1 Motivation and Scope

Ultrasonic imaging (UI) is a prevalent nondestructive testing (NDT) technology [1], which has been widely used for medical imaging [2], temperature sensing [3], structural health monitoring [4], mechanical quality inspection [5], and defect detection in construction materials [6], etc. Recently, advanced signal processing techniques for UI have been applied to characterize mechanical properties, such as strength and elastic modulus [7–10]. However, the performances of these aforementioned techniques are often hindered by the fact that most of them require the *a priori* knowledge about the propagating ultrasonic signals or the testing material samples and the manual operations to calculate essential parameters. As more and more high-performance applications of these materials are being developed, people encounter great challenges in material stress-state detection using UI [11, 12]. As a result, novel blind and automatic signal processing techniques for structural-material stress-state detection in the absence of any *a priori* knowledge or human effort are in high demand [13]. In practice, when ultrasonic signals propagate through the steel materials, there exist multiple signal reflections, attenuations, the interferences between reflected signals and resonances.

Therefore, how to make full use of these signal information for NDT is a primary research interest in the literature. The mathematical representation of the ultrasonic signals given by [13] could be deemed a success since the experimental results have shown that it can lead to more robust methods than those based on the *Gabor* (see [14]) and *Wavelet* (see [15]) transforms, both of which are often used in the existing literature. Especially, when the mismatch between the actual signal and the chosen Gabor window function in [14] (or the chosen scaling function in [15]) is apparent, the signal model presented in [13] would be more "accurate". In our previous work, a *blind signature-signal-extraction based multiridge detection* (BSSEM) method was proposed [13]. This technique is robust over many experimental data since the extracted crucial feature, or "signature signal", is "data-dependent". The only research problem addressed in [13] was the "blind multiridge detection". That is, only the peak location of each ultrasonic echo has been spotted automatically by the computer. How to extract the "effective echoes" still remains challenging. On the other hand, *yield* or *yield zone* detection is an important NDT application for structural health assessment. It has been discovered that the *average energy* over the "effective echoes" (in "good" signal quality) is a robust feature for yield detection in steel structures [16]. Nevertheless, this average energy feature requires exhaustive manual data acquisition, which is very inconvenient to those who perform the NDT for yield detection, especially when prompt reliable decisions are needed.

This thesis makes the first-ever attempt to design a *totally-blind* and *automatic* steel-structure yield-detection mechanism, which requires neither the *a priori* information about the signal nor the human effort in calibration, operation, or data analysis. According to numerous simulation results, our previously proposed BSSEM technique outperforms the

wavelet-based peak detection method for the multiridge detection. Incorporated with the *zero-crossing rate* thresholding method, the BSSEM scheme can be adopted as a robust preprocessor to identify all the echoes in terms of their starting and terminal time points. With the spotted end-points for each echo, the computer-aided system may easily estimate the corresponding signal qualities, namely the *a priori* and *a posteriori* signal-to-noise ratios and automatically extract the effective echoes having satisfactory signal qualities. Then, the average energy can be easily calculated over these effective echoes. Finally, we will compare our proposed computer-aided automatic yield detection method with the conventional method based on the manual operations. It can be observed that the performance reflected by *receiver-operating characteristic* (ROC) curves of our proposed method is very close to that of the conventional technique based on the manual operations. Hence one may save much human effort in the sacrifice of very little detection accuracy by using our proposed new system.

1.2 Thesis Outline

This thesis is organized as follows. In Chapter 2, the mathematical model for the ultrasonic signals collected by the pulse-echo transducers is introduced. In Chapter 3, the multiridge detection algorithms using the BSSEM method [13] and the wavelet-based peak detection scheme are presented. In Chapter 4, a *zero-crossing rate* thresholder is used to detect the starting and terminal points of each ultrasonic signal echo. Then, three signal-to-noise ratio (SNR) measures, namely *a priori SNR*, *a posteriori SNR*, and *average echo SNR* are defined subject to the spotted starting and terminal time points. Furthermore, the *automatic yield*

detection method and the ROC analysis will also be provided in Chapter 4. The procedure and the system diagram for the complete automatic yield detection method are manifested in Chapter 5. Simulation results to justify the effectiveness of our proposed new yield detection method are demonstrated in Chapter 6. Conclusion will be drawn in Chapter **??**, finally.

Nomenclatures: The sets of all integer, real and complex numbers are denoted by $\mathcal{Z}$, $\mathcal{R}$, and $\mathcal{C}$, respectively. Note that the symbol j is reserved as $j \stackrel{\text{def}}{=} \sqrt{-1}$ throughout this thesis.

2. MATHEMATICAL MODEL FOR ULTRASONIC SIGNALS

The basic ultrasonic signal model in this thesis follows [13]. The continuous-time ultrasonic signal $X(t)$ collected by the pulse-echo transducers can be formulated as

$$X(t) = \sum_{i=1}^{L} \varpi_i(t) \cos(\Omega_0 t + \theta_i) + \eta(t), \quad -\infty < t < \infty, \tag{2.1}$$

where $\varpi_i(t)$ is the envelop waveform due to the reflection by the interface of two layers (the interface of inhomogeneities); Ω_0 is the center frequency of the ultrasonic oscillating signal; θ_i is the phase offset due to the i^{th} interface, and $\eta(t)$ is the additive noise. The discrete-time samples of the ultrasonic signal formulated by Eq. (2.1) are written as

$$x(n) = \sum_{i=1}^{L} w_i(n) \cos(\omega_0 n + \theta_i) + \nu(n), \tag{2.2}$$

where $t = n/F_s$, $x(n) \stackrel{\text{def}}{=} X(n/F_s)$, $\nu(n) \stackrel{\text{def}}{=} \eta(n/F_s)$, $\omega_0 \stackrel{\text{def}}{=} \Omega_0/F_s$, $w_i(n) \stackrel{\text{def}}{=} \varpi_i(n/F_s)$, $n \in \mathcal{Z}$, and F_s is the sampling frequency. According to the empirical observation in [17], the discrete-time envelop waveforms $w_i(n), 1 \leq i \leq L$, generally have the following characteristics: $w_i(n), 1 \leq i \leq L$, are the finite-duration window truncation sequences with unique peaks. In other words, $w_i(n)$ is a monotonically increasing function prior to the occurrence of the peak and is a monotonically decreasing function successive to the occurrence of the

peak, $\forall i$. Besides,

$$w_i(n) \begin{cases} \neq 0, & p_i \leq n \leq q_i, \\ \\ = 0, & \text{otherwise}, \end{cases} \tag{2.3}$$

where $p_i, q_i \in \mathcal{Z}$. The discrete-time Fourier transform of $w_i(n)$, for $i = 1, 2, \ldots, L$, is given by

$$W_i(\omega) \stackrel{\text{def}}{=} \sum_{-\infty}^{\infty} w_i(n) e^{-j\omega n}, \tag{2.4}$$

which is a low-pass, narrow-band spectrum such that

$$\frac{\int_{-\omega_{B,i}}^{\omega_{B,i}} |W_i(\omega)|^2 \, d\omega}{\int_{-\pi}^{\pi} |W_i(\omega)|^2 \, d\omega} \geq \xi, \tag{2.5}$$

where ξ is the *energy-percentage coefficient* assumed to be close to 100% and $\omega_{B,i} \ll \omega_0$. Hence, the ultrasonic signal formulated by Eq. (2.2) can be described as a finite-duration, pulse-shaped sinusoid, which is very similar to the modulated digital communication signals [18]. Once the sinusoidal waveform $\cos(\omega_0 n + \theta_i)$ is given, the pulse function $w_i(n)$ can be extracted by a frequency down-converter and a low-pass filter. However, in this ultrasonic signal detection problem, all parameters ω_0, θ_i, p_i, q_i, $\omega_{B,i}$, L, associated with $x(n)$ and $w_i(n), 1 \leq i \leq L$, are unknown; therefore, the conventional demodulation technique cannot be applied. Thus, the BSSEM (*blind-signature-signal-extraction based multiridge detection*) method in [13] without any need of manual operation is considered here for the arbitrary material samples and it can automatically estimate the number of the interfaces (the number of the peaks) $\hat{L}$ and detect the peak locations as

$$\hat{n}_{\max,i} = \arg\max_{n} \left\{ w_i(n) \cos(\omega_0 n + \theta_i) \right\}, \;\; 1 \leq i \leq \hat{L}. \tag{2.6}$$

3. MULTIRIDGE DETECTION USING BSSEM- AND WAVELET- BASED METHODS

In this chapter, two popular multiridge detection methods, namely BSSEM- and wavelet-based schemes, will be addressed for ultrasonic NDT. The implementation procedures of these two methods will be presented here. The simulation results for comparison will be demonstrated in Chapter 6 instead.

3.1 Multiridge Detection Using the BSSEM Method

In our previous work, a *blind multiridge detection* method in the absence of *a priori* knowledge about the materials and manual operation was proposed in [13]. The related details are manifested in the subsequent subsections.

3.1.1 Signature Signal Extraction

The waveforms of ultrasonic signals generated by the transducers would vary a lot over different material samples. Besides, to obtain the *a priori* knowledge regarding the *precise frame functions* $w_i(n)$ and the *precise modulation sinusoids* $\cos(\omega_0 n + \theta_i)$ for a wide variety of materials would be unrealistic [14, 15]. Therefore, we previously designed a novel data-dependent method to blindly extract the signature signal, namely the signal segment $\psi(n)$

containing the dominant peak, which is given by

$$\psi(n) \stackrel{\text{def}}{=} w_1(n)\cos(\omega_0 n + \theta_1), \tag{3.1}$$

where $w_1(n_{\max,1}) \geq w_i(n_{\max,i}), \forall i \neq 1$.

3.1.2 Energy Features for Signature Signal Spotting

According to [13], the signature signal $\psi(n)$ can be spotted using the *framed energy*, which depends on the frame size and can be considered as the transformation from the original ultrasonic signal sequence, i.e., $x(n), n \in \mathcal{Z}, \xrightarrow{\Gamma_{N_f,\Delta}} E_{N_f,\Delta}(k), k \in \mathcal{Z}$. It is defined as:

$$E_{N_f,\Delta}(k) = \Gamma_{N_f,\Delta}[x(n)] \stackrel{\text{def}}{=} \frac{1}{N_f} \sum_{n=(k-1)\Delta+1}^{(k-1)\Delta+N_f} x^2(n), \tag{3.2}$$

where N_f is the energy-frame size, Δ is the frame forwarding size, and k is the frame index. One should note that with a proper N_f, the framed energy sequence would be a smooth function (monotonically increasing then monotonically decreasing) in the presence of signature sequence. However, there exists a *frame-size dilemma* for generating the framed energy sequence $E_{N_f,\Delta}(k)$. This dilemma will be discussed as follows.

3.1.3 Frame-Size Dilemma

The optimal multiridge detection can be achieved when the energy sequence $E_{N_f,\Delta}(k)$ has a "least spiky" shape in each individual ridge interval $[p_i, q_i]_{i=1,2,\ldots,L}$, which is quite sensitive to the frame size N_f. According to [13], the discrete-time Fourier transform of $E_{N_f,\Delta}(k)$ is denoted by $\Xi_{N_f,\Delta}(\omega)$, which satisfies

$$|\Xi_{N_f,\Delta}(\omega)| \leq \frac{1}{N_f} \sum_{i=1}^{L} \sum_{n=p_i}^{q_i} w_i^2(n)\cos^2(\omega_0 n + \theta_i)|\Psi_n(\omega)|, \tag{3.3}$$

where

$$\Psi_n(\omega) \stackrel{\text{def}}{=} \frac{\sin\left(\frac{\omega}{2}\left(\left\lfloor\frac{N_f-1}{\Delta}\right\rfloor+b\right)\right)}{\sin(\frac{\omega}{2})} \times \exp\left(-j\frac{\omega}{2}\left(\left\lfloor\frac{n-1}{\Delta}\right\rfloor+\left\lceil\frac{n-N_f}{\Delta}\right\rceil+2\right)\right). \quad (3.4)$$

From the inequality in Eq. (3.3), we know that the sidelobes of $\left|\Xi_{N_f,\Delta}(\omega)\right|$ for $|\omega| \geq (2\pi/\lfloor N_f - 1/\Delta\rfloor + b)$ are relatively small compared to the DC frequency component $\left|\Xi_{N_f,\Delta}(0)\right|$. As a result, its bandwidth can be roughly approximated by $(4\pi/\lfloor N_f - 1/\Delta\rfloor + b)$, which means that the larger N_f , the smoother the framed energy $\left|\Xi_{N_f,\Delta}(\omega)\right|$ since there will exist fewer high-frequency components. However, if N_f is too large, the bandwidth of $\left|\Xi_{N_f,\Delta}(\omega)\right|$ will be very small, i.e., $E_{N_f,\Delta}(k)$ appears to be a constant sequence and cannot provide informative features for reliable ridge detection.

3.1.4 Optimal Frame-Size Determination

From the discussion in previous subsections, the *optimal frame-size* for a framed-energy sequence $E_{N_f,\Delta}(k)$ can be achieved when it appears to have a both smooth (with a large N_f) and compact-duration shape (with a small N_f). An algorithm can be found in [13] to seek the trade-off between these two goals by a nonlinear program to optimize the frame size N_f subject to the constraint of a compact-duration $E_{N_f,\Delta}(k)$. We adopt the *kurtosis function* $\text{kur}(E_{N_f,\Delta}(k))$ (see [19]) to construct a new constraint function. Given a frame size N_f and a frame forwarding size Δ, the constraint function is

$$\text{kur}\left(E_{N_f,\Delta}(k)\right) \stackrel{\text{def}}{=} \frac{\sum_k P_k\left[(k-1)\Delta+1-M\right]^4}{\left(\sum_k P_k[(k-1)\Delta+1-M]^2\right)^2}, \quad (3.5)$$

where P_k is the sequence satisfying the probability axioms (see [19]) and it is defined as

$$P_k \stackrel{\text{def}}{=} \frac{E_{N_f,\Delta}(k)}{\sum\limits_k E_{N_f,\Delta}(k)}, \tag{3.6}$$

with the *mean* M given by

$$M \stackrel{\text{def}}{=} \sum_k P_k[(k-1)\Delta + 1]. \tag{3.7}$$

The kurtosis measure, given by Eq. (3.5), is Δ *multiple-shift invariant*, i.e., one can start to collect the signal features at anytime for the mechanical property characterization. Consequently, the optimal frame size N_f^* can be obtained according to the following criterion:

$$N_f^* = \max(N_f)$$

subject to

$$\frac{\left|\text{kur}(E_{N_f,\Delta}(k)) - \text{kur}(E_{N_f+\delta N,\Delta}(k))\right|}{\text{kur}(E_{N_f,\Delta}(k))} \leq \kappa_{th}, \tag{3.8}$$

where κ_{th} is the pre-determined upper-bound for the underlying kurtosis sensitivity constraint function and δN is the incremental frame size.

3.1.5 Blind Signature Signal Extraction

When the optimal frame-size N_f^* is achieved from Eq. (3.8), one can construct the energy sequence $E_k \stackrel{\text{def}}{=} E_{N_f^*,\Delta}(k)$ with $N_f = N_f^*$. We assume that the k_p^{th} frame in E_k contains the peak value of the signature signal $\psi(n)$, where $k_p = \arg\max\limits_k(E_k)$. Then, the duration $[p_1, q_1]$ of the signature signal $\psi(n) = w_1(n)\cos(\omega_0 n + \theta_1)$ can be estimated as

$$\begin{aligned} \hat{p}_1 &= (k_s - 1)\Delta + 1, \\ \hat{q}_1 &= (k_e - 1)\Delta + N_f^*, \end{aligned} \tag{3.9}$$

where k_s, k_e are the first energy frames satisfying $E_{k_s} < \epsilon_{th}$ and $E_{k_e} < \epsilon_{th}$ during the count-down and the count-up, respectively, starting from the frame index k_p; is the pre-determined energy threshold. According to Eq. (3.9), the signature signal can be extracted as

$$\hat{\psi}(n) = \begin{cases} x(n), & \hat{p}_1 \le n \le \hat{q}_1 \\ 0, & \text{elsewhere} \end{cases}, \tag{3.10}$$

and the peak location $\hat{n}_{\max,1}$ in the signature signal can be estimated as

$$\hat{n}_{\max,1} = \arg\max_n \left[\hat{\psi}(n)\right]. \tag{3.11}$$

3.1.6 Blind Multiridge Detection

Since both L and $\hat{n}_{\max,i}$ are unknown, we apply the normalized cross-correlation function $\gamma^{\mathrm{B}}(m)$ between $x(n)$ and $\hat{\psi}(n-m)$ to determine L and $\hat{n}_{\max,i}, i = 2, 3, \ldots, L$, such that

$$\gamma^{\mathrm{B}}(m) \stackrel{\text{def}}{=} \frac{r^{\mathrm{B}}_{x\hat{\psi}}(-m)}{\sqrt{\sum_n \hat{\psi}^2(n)}\sqrt{\sum_n x^2(n)}}, \qquad m = 0, 1, 2, \ldots, \tag{3.12}$$

where $r^{\mathrm{B}}_{x\hat{\psi}}(-m) \stackrel{\text{def}}{=} \sum_n x(n)\hat{\psi}(n-m)$ is the cross-correlation function between the entire signal $x(n)$ and the estimated signature $\hat{\psi}(n)$. Sort $\left|\gamma^{\mathrm{B}}(m)\right|$ in a descending order (with the re-ordered index sequence $m_1, m_2, \ldots, m_C, \ldots$) which satisfies the following inequality:

$$\left|\gamma^{\mathrm{B}}(m_l)\right| < \zeta_{th}, \quad \text{for } \; l = C+1, C+2, C+3, \ldots, \tag{3.13}$$

where ζ_{th} is the absolute cross-correlation coefficient threshold. Seek the subset B^{B} among the indices $(m_1, m_2, \ldots, m_C)$, which contains no adjacent ridges within the ridge resolution $\delta n_{\max}$ such that

$$B^{\mathrm{B}} \stackrel{\text{def}}{=} \{l : |m_l - m_{l'}| > \delta n_{\max}; l, l' = 1, 2, \ldots, C; l \neq l'\}. \tag{3.14}$$

The size of B^{B} is the number of the ridges to be detected. Thus, each peak location can be estimated as

$$\hat{n}_{\max,i} = \arg\max_{n\in\left[m_{B^{\mathrm{B}}(i)}-\frac{\delta n_{\max}}{2}+1, m_{B^{\mathrm{B}}(i)}+\frac{\delta n_{\max}}{2}-1\right]} \{x(n)\}, \quad \text{for } i = 1, 2, \ldots, \hat{L}, \tag{3.15}$$

where $B^{\mathrm{B}}(i)$ denotes the i^{th} element of the set B^{B}.

3.1.7 Summarized BSSEM Algorithm

Multiridge detection using the BSSEM method can be briefly summarized as follows.

Step 1. Optimal Frame-Size N_f^* Selection: Vary the frame-size N_f on the dyadic scale, namely $N_f = 2^1, 2^2, 2^3, \ldots$. For each N_f, compute the kurtosis function $\mathrm{kur}\left(E_{N_f,\Delta}(k)\right)$ of the framed-energy sequence $E_{N_f,\Delta}(k)$, where Δ is the frame forwarding size, k is the frame index, and $k = 1, 2, \ldots$. Then determine the optimal frame size N_f^* according to Eq. (3.8).

Step 2. Parameter Estimation for the Signature Signal $\hat{\psi}(n)$: Set $N_f = N_f^*$; then estimate the duration $[\hat{p}_1, \hat{q}_1]$ and the peak location $\hat{n}_{\max,1}$ of the signature signal $\hat{\psi}(n)$ according to Eqs. (3.9)-(3.11).

Step 3. Construction of the Normalized Cross-Correlation Function $\gamma^{\mathrm{B}}(m)$: Construct the normalized cross-correlation function $\gamma^{\mathrm{B}}(m)$ according to Eq. (3.21), between the ultrasonic signal $x(n)$ and the estimated signature signal $\hat{\psi}(n)$.

Step 4. Determination of the Number of Ridges $\hat{L}$: Form the sample index sequence $(m_1, m_2, ..., m_C)$ according to the sort-and-select procedure in Eqs. (3.23)-(3.26). Remove the spurious ridges within the ridge resolution and construct a set B^{B} of sample indices corresponding to the true ridges. Then the number of the ridges $\hat{L}$ can be determined by the size of B^{B}, namely $\left|B^{\mathrm{B}}\right|$.

Step 5. Detection of Peak Locations $\hat{n}_{\max,i}, i = 1, 2, ..., \hat{L}$*:* The peak locations $\hat{n}_{\max,i}, i = 1, 2, ..., \hat{L}$, can be obtained according to the peak location search procedure in Eq. (3.11).

In our previous work in [13], although the BSSEM method performed quite well for blind multiridge detection in composite materials, it cannot be applied for yield detection at all. We need to employ the BSSEM technique as the preprocessor and incorporate it with other sophisticated mechanisms for the purpose of yield detection, such as the new mechanism for automatically estimating the starting and terminal time points of each ultrasonic signal echo (in terms of $x(n)$, $p_i \leq n \leq q_i$). To ensure that the BSSEM based preprocessor is robust over the multiridge detection system using the popular wavelets, we present the wavelet-based multiridge detection scheme in the following section for comparison.

3.2 Multiridge Detection Using Wavelets

Other than our previously proposed BSSEM method, commonly-used peak detection methods include *threshold peak detection*, *curve-fitting-based peak detection* and *wavelet-based peak detection* [20]. The wavelet-based peak detection method was deemed more robust and accurate than the other two existing methods since it utilizes the inherent multiscale nature of wavelet analysis [20]. Hence in this thesis, the mainstream wavelet-based peak detection method will be compared with our proposed BSSEM method.

According to [20], when an appropriate *mother wavelet* is well selected, the wavelet-based peak detection method is quite robust against noise. *Wavelet transform* (WT) specifies the correlation between a signal and a set of wavelet basis. Usually, a *square-integrable* mother wavelet $h(t)$ is picked and a set of sub-wavelets $h_{a,b}(t)$ is engendered from the mother wavelet

by a *dilation factor* $a > 0$ and a *translation factor* $b \in \mathcal{R}$. So the *WT expansion coefficients* $W_X(a,b)$ of the continuous-time signal $X(t)$ are given by

$$W_X(a,b) \stackrel{\text{def}}{=} \int_{-\infty}^{\infty} X(t)\, h_{a,b}^*(t)\, dt = X(t) \otimes \frac{h^*(t/a)}{\sqrt{a}}, \tag{3.16}$$

where * is the conjugate operator and $\otimes$ denotes the *linear convolution*, and $h_{a,b}(t)$ is defined as

$$h_{a,b}(t) \stackrel{\text{def}}{=} \frac{1}{\sqrt{a}}\, h\left(\frac{t-b}{a}\right). \tag{3.17}$$

In the frequency domain, Eq. (3.17) yields

$$H_{a,b}(f) \stackrel{\text{def}}{=} \sqrt{a}\, H(af)\, e^{j\,2\pi f b}, \tag{3.18}$$

where

$$H(f) \stackrel{\text{def}}{=} \int_{-\infty}^{\infty} h(t)\, e^{-j2\pi f t}\, dt, \tag{3.19}$$

and

$$H_{a,b}(f) \stackrel{\text{def}}{=} \int_{-\infty}^{\infty} h_{a,b}(t)\, e^{-j2\pi f t}\, dt. \tag{3.20}$$

Note that $h_{a,b}(t)$ actually represents the impulse response of a band-pass filter. In many applications, the signal is sampled as $x(n)$ and the dilation factor a as well as the translation factor b are also discretized as $a = a_0^m$, where $a_0 \geq 1$, and $b = nb_0a_0^m$. Similarly, the discretized mother wavelet $h(n) \stackrel{\text{def}}{=} h(n/F_s)$ and the discretized sub-wavelet $h_{a,b}(n) \stackrel{\text{def}}{=} h_{a,b}(n/F_s)$ can also be established, where F_s is the sampling frequency.

The *template matching* technique has been widely adopted for the signal detection among a wide variety of applications [21–23]. In principle, one can match the signal to be detected with a pre-acquired "signal template". Thus, the more reliable this pre-acquired template,

the more accurate the resultant detection rate. The most popular templates (or signal basis function) are wavelets [24–28]. Although there exist a wide variety of wavelets, not all of them are appropriate to characterize the ultrasonic signals. It is critical to select a suitable mother wavelet $h(n)$ so that its sub-wavelet impulse response $h_{a,b}(n)$ can well match the ultrasonic echoes. Thus, the best performance of the wavelet-based peak detection method can be attained [24–28].

Once an appropriate sub-wavelet impulse response $h_{a,b}(n)$ is determined, one can apply the normalized cross-correlation function $\gamma^{\mathrm{W}}(m)$ between the discrete-time signal $x(n)$ and the sub-wavelet $h_{a,b}(n-m)$ to estimate the number of peaks $\hat{L}$ and the peak locations $\hat{n}_{\max,i}, i = 1, 2, \ldots, \hat{L}$ in an ultrasonic signal expressed by Eq. (2.2), such that

$$\gamma^{\mathrm{W}}(m) \stackrel{\text{def}}{=} \frac{r_{xh}(-m)}{\sqrt{\sum_n |h_{a,b}(n)|^2}\sqrt{\sum_n |x(n)|^2}}, \qquad m = 0, 1, 2, \ldots, \tag{3.21}$$

where $r_{xh}(-m) \stackrel{\text{def}}{=} \sum_n x(n)\, h_{a,b}(n-m)$ is the cross-correlation function between the entire signal $x(n)$ and the sub-wavelet impulse response $h_{a,b}(n)$. After $\gamma^{\mathrm{W}}(m)$ is obtained, the indices m should be sorted in an order $(m_1, m_2, m_3, \ldots)$ such that

$$\left|\gamma^{\mathrm{W}}(m_l)\right| > \left|\gamma^{\mathrm{W}}(m_l+1)\right|, \qquad \text{for } l = 1, 2, 3, \ldots. \tag{3.22}$$

Then an absolute cross-correlation coefficient threshold ζ_{th}^{W} is chosen and a set of indices m_l can be formed as $(m_1, m_2, \ldots, m_C)$, which satisfies

$$\left|\gamma^{\mathrm{W}}(m_l)\right| < \zeta_{th}^{\mathrm{W}}, \quad \text{for } l = C+1, C+2, C+3, \ldots. \tag{3.23}$$

We would like to seek the subset B^{W} among the indices $(m_1, m_2, \ldots, m_C)$, which contains

no adjacent ridges within a pre-specified *ridge resolution* $\delta n_{\max}^{\mathrm{W}}$. The subset B^{W} is given by

$$B^{\mathrm{W}} \stackrel{\mathrm{def}}{=} \left\{ l : |m_l - m_{l'}| > \delta n_{\max}^{\mathrm{W}};\ l, l' = 1, 2, \ldots, C;\ l \neq l' \right\}, \tag{3.24}$$

and the number of the ridges can be estimated as

$$\hat{L} = \left| B^{\mathrm{W}} \right|, \tag{3.25}$$

where $\left| B^{\mathrm{W}} \right|$ denotes the number of the elements in the subset B^{W}. Finally, each peak location can be estimated as

$$\hat{n}_{\max,i} = \arg\max_{n \in \left[m_{B^{\mathrm{W}}(i)} - \frac{\delta n_{\max}^{\mathrm{W}}}{2} + 1, m_{B^{\mathrm{W}}(i)} + \frac{\delta n_{\max}^{\mathrm{W}}}{2} - 1 \right]} \{x(n)\}, \qquad \text{for } \ i = 1, 2, \ldots, \hat{L}, \tag{3.26}$$

where $B^{\mathrm{W}}(i)$ is the i^{th} element of the set B^{W}.

In summary, the performance of the wavelet-based peak detection method is very sensitive to the selection of an appropriate mother wavelet and the associated parameters a, b. Nevertheless, all of them are highly data-dependent. Therefore, our proposed BSSEM scheme, which directly extracts the inherent signature from each signal sequence, would often outperform the wavelet-based peak detection method. Simulation results to justify this fact will be presented in Chapter 6.

4. YIELD DETECTION AND THE ROC ANALYSIS

In this thesis, we focus on an important NDT application, yield or yield zone detection, for structural health monitoring. For material yield detection, usually the testing specimens are loaded up to failure at the targeted stress levels at both before and after the *yield zone*. However, the relation between the material stress-state and the characteristics of the ultrasonic signals remains challenging [16]. During the entire stress loaded experiment procedure, changes in the amplitude of the ultrasonic signals are empirically observed, especially when stresses are applied beyond yield. Besides amplitude, we also take some other characteristics of the ultrasonic signals into consideration, which include both time-domain and frequency-domain parameters such as average echo-energies, fast Fourier transform (FFT) coefficients, Chirp-Z transform coefficients, and discrete wavelet transform (DWT) coefficients [16]. According to previous experiments stated in [16], the average echo-energies lead to the best yield-detection performance. Hence in this thesis, we will focus on the approach based on the average echo-energy feature. The *average energy* over the "effective echoes" (in "good" signal quality) has been reported as a robust feature for yield detection in steel structures [16]. However, to the best of my knowledge, there exists no blind or automatic feature extraction method for the yield detection. In this chapter, we will present a novel blind feature extraction (without any need of human operation), which is based on the blind multiridge detection technique stated in Section 3.1.

4.1 Detecting Starting and Terminal Points of Ultrasonic Echoes

A typical ultrasonic signal containing several echoes is illustrated by Figure 4.1. Empirically speaking, the "presence" and "absence" of echoes can be differentiated by the corresponding zero-crossing rates according to Figure 4.1. The zero-crossing rates can be estimated using the "short-time windows". Observing Figure 4.1, one can simply conclude the follows. If there is a sudden substantial decrement in the zero-crossing rate, the beginning of an echo can be identified. On the other hand, if there is a sudden substantial increment in the zero-crossing rate, the end of an echo can be spotted instead. Nevertheless, there still remain some unanswered questions regarding this intuitive approach. How do we select the appropriate short-time window size? How do we select the reliable threshold to reflect the "substantial change" in the zero-crossing rate? If these two problems can be well addressed, then the starting and terminal time points of the echoes can be identified effectively. To answer these two questions, we can rely on the detected ridges which result from the methods in the previous chapter. However, since the BSSEM technique is more robust than the wavelet-based peak detection method, we will focus on the former scheme here. The appropriate window size for calculating the zero-crossings has to be related to the signature signal $\hat{\psi}(n)$ as given by Eq. (3.10). By applying the proposed multiridge detection method in [13], one can obtain all peak locations $\hat{n}_{\max,i}$, $i = 1, 2, \ldots, \hat{L}$, of an ultrasonic signal $x(n)$. Suppose that there are λ signal samples in the signature signal $\hat{\psi}(n)$ from its detected peak $\hat{n}_{\max,1}$ to its first zero-crossing point. Thus, we define the *signature period* as $\Lambda \stackrel{\text{def}}{=} 4\lambda$. Therefore, the corresponding *signature zero-crossing rate* can be defined as $\hat{\Upsilon} \stackrel{\text{def}}{=} 1/\Lambda$. We propose a novel algorithm to automatically identify the starting and terminal points of the ultrasonic echoes

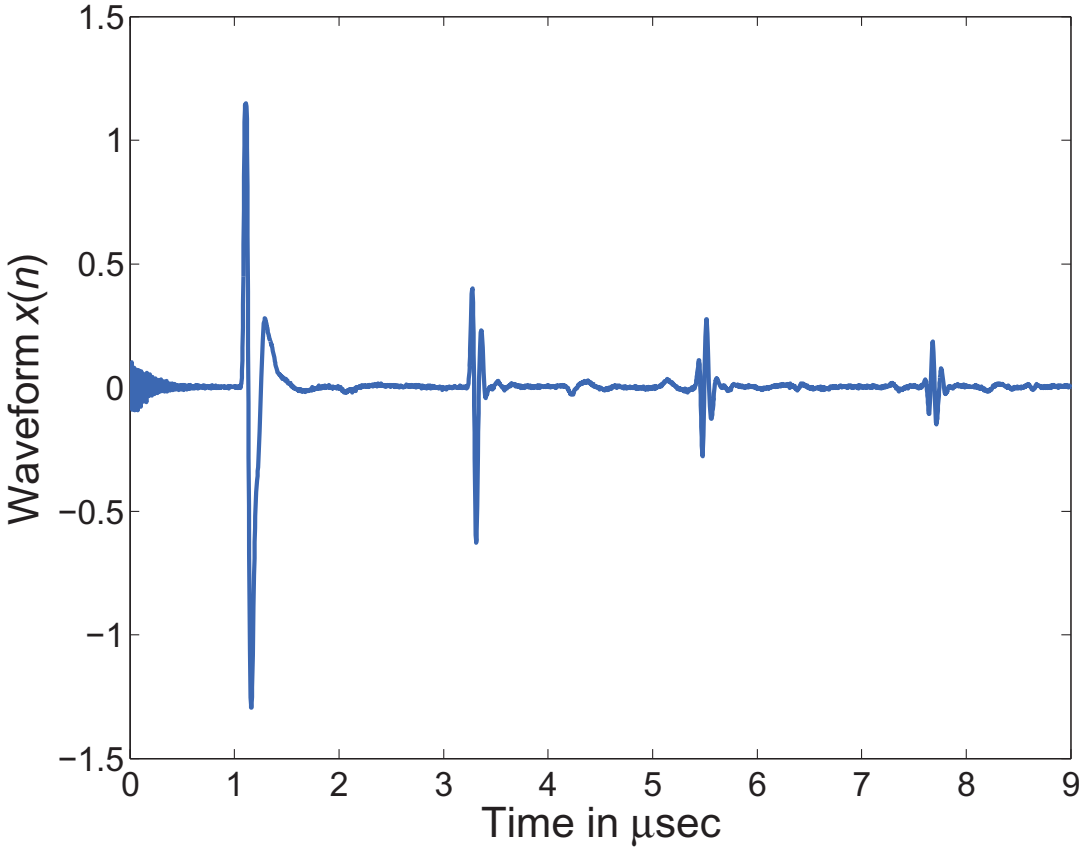

Figure 4.1: A typical ultrasonic signal.

using the zero-crossing estimation. The details are stated in Algorithm 1.

Here we denote ρ_{th} as the *zero-crossing ratio threshold*, which is independent of both sampling rate and material stress-state. Besides, the index set of zero-crossings is denoted by $\Theta(n)$ subject to the window of size Λ, where $|\Theta(n)|$ is the number of elements in $\Theta(n)$. If $|\Theta(n)|$ is decreasing with respect to n until $|\Theta(n)| \leq \rho_{th}\hat{\Upsilon}$, an ultrasonic echo is assumed to start. On the other hand, if $|\Theta(n)|$ is increasing with respect to n until $|\Theta(n)| \geq \rho_{th}\hat{\Upsilon}$, an ultrasonic echo is assumed to end. Note that $\lfloor\,\rfloor$ is the *integer rounding-down* operator. For example, applying Algorithm 1 for the ultrasonic signal shown in Figure 4.1, one can obtain the starting and terminal time points of each echo as shown in Figure 4.2 (denoted by red $*$).

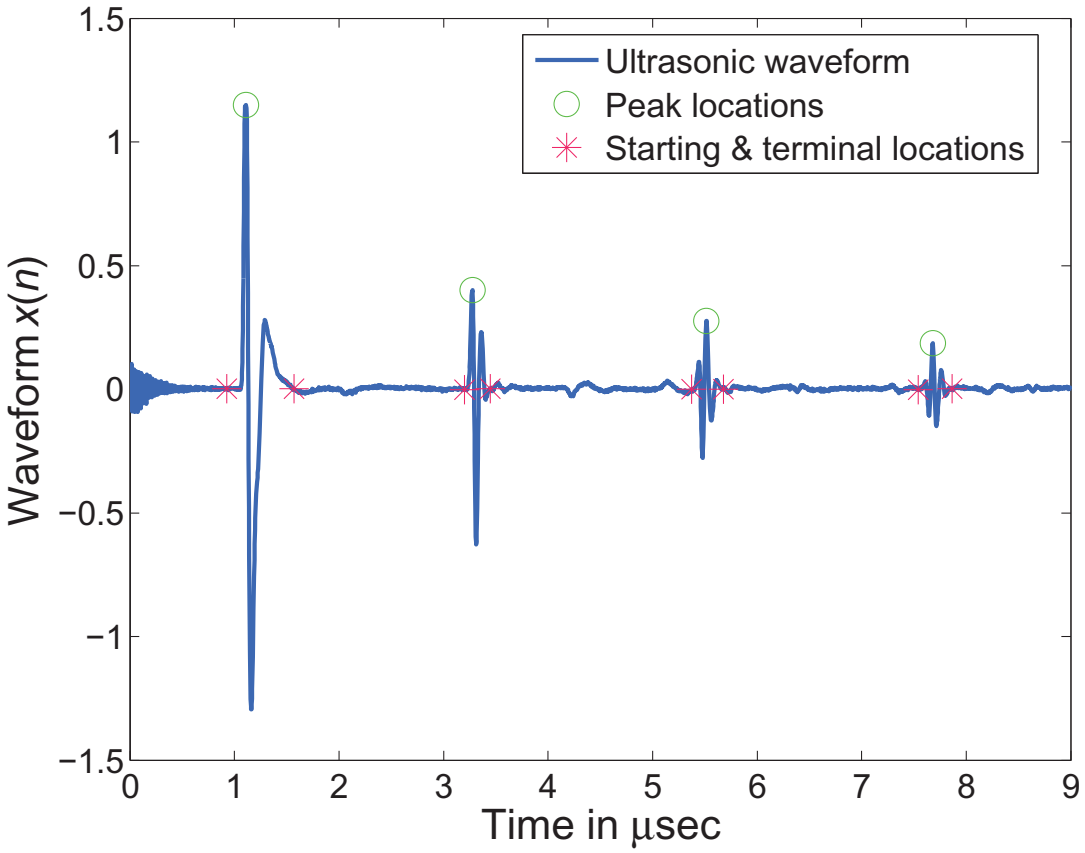

Figure 4.2: Detected starting and terminal time points using the zero-crossing rates.

Algorithm 1 Starting & Terminal Point Estimation Algorithm

Input:

Ultrasonic signal, $x(n)$;
Signal length (of $x(n)$) $\mathcal{N}$;
Peak locations of the ultrasonic signal, $\hat{n}_{\max,i}$, $i = 1, 2, \ldots \hat{L}$, resulting from the BSSEM method in [13];
Signature period, Λ;
Zero-crossing ratio threshold, ρ_{th};
Signature zero-crossing rate, $\hat{\Upsilon}$;

Output:

Detected starting points for all echoes, $\hat{p}_i, i = 1, 2, \ldots \hat{L}$;
Detected terminal points for all echoes, $\hat{q}_i, i = 1, 2, \ldots \hat{L}$;

Construct the adjacent peak location pairs, $(\hat{n}_{\max,i}, \hat{n}_{\max,i+1}), i = 1, 2, \ldots, \hat{L} - 1$;
for $i = 1; i < \hat{L}; i++$ **do**
  for $n = \hat{n}_{\max,i}; n < \hat{n}_{\max,i+1} - \Lambda; n++$ **do**
    for $\mu = 0; \mu < \Lambda; \mu++$ **do**
      $c(\mu + 1) = x(n + \mu)\, x(n + \mu + 1)$;
    end for
    $\Theta(n) \stackrel{\text{def}}{=} \{\mu \mid c(\mu + 1) < 0\}$;
    if $|\Theta(n)| < \rho_{th}\hat{\Upsilon}$ **then**
      Go to Step 3;
    else
      $\hat{q}_i = n + \left\lfloor \frac{\Lambda}{2} \right\rfloor$;
      Go to Step 15;
    end if
  end for
  for $n = \hat{n}_{\max,i+1}; n > \hat{n}_{\max,i} + \Lambda; n--$ **do**
    for $\mu = 0; \mu < \Lambda; \mu++$ **do**
      $c(\mu + 1) = x(n - \mu)\, x(n - \mu - 1)$;
    end for
    $\Theta(n) \stackrel{\text{def}}{=} \{\mu \mid c(\mu + 1) < 0\}$;
    if $|\Theta(n)| < \rho_{th}\hat{\Upsilon}$ **then**
      Go to Step 15;
    else if $i < \hat{L} - 1$ **then**
      $\hat{p}_{i+1} = n - \left\lfloor \frac{\Lambda}{2} \right\rfloor$;
      Go to Step 2;
    else
      $\hat{p}_{i+1} = n - \left\lfloor \frac{\Lambda}{2} \right\rfloor$;
      Go to Step 31;
    end if
  end for
end for
Repeat Steps 3-14 for $\hat{n}_{\max,i} = \hat{n}_{\max,\hat{L}}$ and $\hat{n}_{\max,i+1} = \mathcal{N}$ except that $\hat{q}_{\hat{L}} = n + \left\lfloor \frac{\Lambda}{2} \right\rfloor$ is forcefully set;
Repeat Steps 15-29 for $\hat{n}_{\max,i} = 1$ and $\hat{n}_{\max,i+1} = \hat{n}_{\max,1}$ except that $\hat{p}_1 = n - \left\lfloor \frac{\Lambda}{2} \right\rfloor$ is forcefully set;
return $\hat{p}_i$ and $\hat{q}_i$, for $i = 1, 2, \ldots \hat{L}$.

4.2 Echo Quality-Average SNR

After estimating the starting and terminal points of each echo using the proposed technique in Section 4.1, namely $\hat{p}_i$ and $\hat{q}_i$, for $i = 1, 2, \ldots \hat{L}$, now we can measure the *a priori* SNR as $\mathcal{SNR}_{\text{pri},i}$ and the *a posteriori* SNR as $\mathcal{SNR}_{\text{post},i}$ for each ultrasonic echo accordingly. They are

$$\begin{aligned} \mathcal{SNR}_{\text{pri},i} &\stackrel{\text{def}}{=} \frac{\sum_{n=\hat{p}_i}^{n=\hat{q}_i} |x(n)|^2}{\sum_{n=\hat{q}_{i-1}}^{n=\hat{p}_i} |x(n)|^2}, \qquad i = 2, 3, \ldots, \hat{L}, \\ \mathcal{SNR}_{\text{post},i} &\stackrel{\text{def}}{=} \frac{\sum_{n=\hat{p}_i}^{n=\hat{q}_i} |x(n)|^2}{\sum_{n=\hat{q}_i}^{n=\hat{p}_i+1} |x(n)|^2}, \qquad i = 1, 2, \ldots, \hat{L} - 1. \end{aligned} \tag{4.1}$$

We may further define the average SNR for each ultrasonic echo as $\overline{\mathcal{SNR}}_i$, which is the mean of the corresponding *a priori* and *a posteriori* SNRs, such that

$$\overline{\mathcal{SNR}}_i \stackrel{\text{def}}{=} \frac{\mathcal{SNR}_{\text{pri},i} + \mathcal{SNR}_{\text{post},i}}{2}, \quad i = 2, 3, \ldots, \hat{L} - 1, \tag{4.2}$$

while

$$\begin{aligned} \overline{\mathcal{SNR}}_1 &\stackrel{\text{def}}{=} \mathcal{SNR}_{\text{post},1}, \\ \overline{\mathcal{SNR}}_{\hat{L}} &\stackrel{\text{def}}{=} \mathcal{SNR}_{\text{pri},\hat{L}}. \end{aligned} \tag{4.3}$$

In practice, the average SNR $\overline{\mathcal{SNR}}_i$ can be used as the essential feature and compared with a pre-selected threshold (dependent on individual material properties) to determine which echoes are "effective". As a matter of fact, $\overline{\mathcal{SNR}}_i$ should be monotonically decreasing with respect to echo index i due to signal attenuation, i.e., $\overline{\mathcal{SNR}}_i > \overline{\mathcal{SNR}}_j$, where $1 \leq i < j \leq \hat{L}$. When $\overline{\mathcal{SNR}}_i$ is rather small, the signal energy level is very close to the background noise level and such an echo is useless for yield detection. Consequently, we define $\mathcal{SNR}_{th}$ as the

SNR threshold to pick the m^* effective (preceding) echoes such that

$$\begin{aligned} \overline{\mathcal{SNR}}_{m^*} &\geq \mathcal{SNR}_{th}, \\ \overline{\mathcal{SNR}}_{m^*+1} &< \mathcal{SNR}_{th}, \end{aligned} \tag{4.4}$$

where $1 \leq m^* < \hat{L}$.

4.3 Feature Extraction for Yield Detection

According to the technique presented in Section 4.2, we may acquire m^* effective echoes. The average energy E for these effective echoes in the ultrasonic signal $x(n)$ can be obtained as

$$E \stackrel{\text{def}}{=} \frac{1}{m^*} \sum_{i=1}^{m^*} \sum_{n=\hat{p}_i}^{\hat{q}_i} |x(n)|^2, \tag{4.5}$$

where $\hat{p}_i$ and $\hat{q}_i$ are the identified starting and terminal time points for the i^{th} echo according to Algorithm 1. One may perform the yield detection for steel materials using the feature given by Eq. (4.5). A simple threshold detector was proposed by [16] subject to manual operation. Nevertheless, we may automatically (blindly) extract this feature according to the proposed schemes in Sections 3, 4.1, and 4.2 to facilitate a novel and user-friendly pre-processor for the subsequent detection mechanism. The remaining task for yield detection is simply to select the appropriate threshold for the feature parameter E. We will present the threshold determination procedure in the following section.

4.4 Receiver Operating Characteristics Analysis

Both statistical analysis and experimental results show that there are clear distinctions between pre- and post-yielding of specimen materials for the average-energy features [16]. As a result, the intense changes in average energies between these two states can be used to determine the threshold for yield detection, which would lead to the optimum detection [16]. According to [16], the *ROC analysis* can be employed to determine the optimal threshold value. ROC analysis is a two-dimensional graphical technique for people to optimize the classifiers [29], and it has plenty of applications such as medical-diagnosis decision-making and computer-network filter-performance evaluation [30, 31]. ROC analysis is performed on both sets of data, namely *positives* and *negatives*. Based on these data, an *ROC curve* can be delineated as the *correct detection rate* (CDR) versus the *false detection rate* (FDR) subject to the varying threshold [32]. Suppose that $\mathcal{CDR}$ and $\mathcal{FDR}$ represent CDR and FDR, respectively. They are

$$\begin{aligned} \mathcal{CDR} &= \frac{\text{Correctly Classified Positives}}{\Phi_P}, \\ \mathcal{FDR} &= \frac{\text{Incorrectly Classified Negatives}}{\Phi_N}, \end{aligned} \tag{4.6}$$

where Φ_P and Φ_N denote the total numbers of positives and negatives, respectively.

The performance of a classifier (detector) is measured by how close its ROC curve is to the upper left corner of the graph or how far its ROC curve is from the $x = y$ line, which corresponds to the classifiers that are basically nothing better than tossing a coin randomly. Moreover, another way of measuring the performance of a classifier is calculating the area under its ROC curve as a scalar parameter (see [33]) and denote this area by $\mathcal{AUC}$. It means that the classification (detection) performance improves when $\mathcal{AUC}$ becomes closer and closer

to one. In practise, no practical classifier has an $\mathcal{AUC}$ value less than 0.5, which is produced by the diagonal ROC line $x = y$ [29]. More details about how to determine the optimal threshold for classifying the stress-states of steel materials using the ROC analysis can be found in [16]. After obtaining the optimal classification threshold ϑ_{th} from the training data set according to [16], one may classify the stress-states for any specimen material simply by comparing the average energy E with this threshold such that

$$E \begin{array}{c} \text{before yield} \\ > \\ < \\ \text{after yield} \end{array} \vartheta_{th} \tag{4.7}$$

5. SUMMARIZED AUTOMATIC YIELD DETECTION METHOD

Based on the discussions in Sections 3-4, the complete automatic (blind) yield detection procedure can be summarized as follows:

Step 1. Preprocessing: According to the BSSEM method in [13], seek the peak locations, namely $\hat{n}_{\max,i}$, $i = 1, 2, ..., \hat{L}$, of the ultrasonic signal as illustrated in Section 3.1.

Step 2. Echoes' Starting and Terminal Points Estimation: Given the spotted peak locations $\hat{n}_{\max,i}$, $i = 1, 2, ..., \hat{L}$, estimate the starting and terminal time points $(\hat{p}_i, \hat{q}_i)$, $i = 1, 2, \ldots, \hat{L}$ according to Algorithm 1.

Step 3. Average SNR Calculation: Calculate the *a prior* and *a posteriori* SNRs of each echo according to Eq. (4.1). Then take the average SNR $\overline{\mathcal{SNR}}_i$ for each echo $i = 1, 2, \ldots, \hat{L}$, according to Eq. (4.2) and Eq. (4.3).

Step 4. Determination of Effective Echoes' Number: Given the SNR threshold $\mathcal{SNR}_{th}$, determine the number of effective echoes m^* according to Eq. (4.4) for further feature extraction.

Step 5. Average Energy Computation: Given the number of effective echoes m^*, calculate the average energy E according to Eq. (4.5).

Step 6. Yield Detection Using the ROC Analysis: Apply the ROC technique to obtain the optimal classification threshold ϑ_{th} from the training data. Compare it with the average

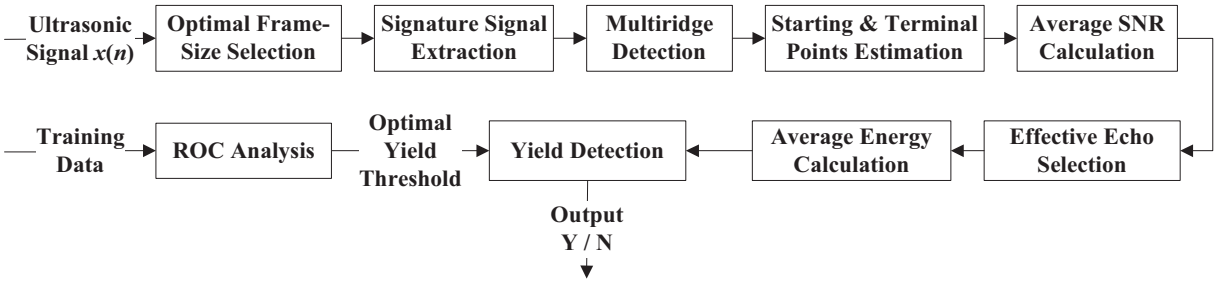

Figure 5.1: System diagram of the new proposed novel automatic yield detection mechanism.

energy E (feature parameter) and then determine the stress state (before or after yield) of the material specimen based on Eq. (4.7).

The complete procedure is illustrated by the flowchart depicted in Figure 5.1.

6. SIMULATION

The complete ultrasonic testing setup for the through-transmission (TT) test mode and the assembly for the main units of the system are illustrated in Fig. 6.1. In this experiment, four batches of Grade-36 dog-bone shaped specimens were obtained from cutting four kinds of steel plates by a hydrocut water-jet machine. The thicknesses of these specimens varied from 1/8 to 3/8 inches. Other dimensions were the dimensions of the rectangular sheet-type specimen complying with ASTM Standard E8-04 [34], which are shown in Fig. 6.2.

The specimens were classified into four groups based on the thickness of the plates. Note that even though these plates were supposed to possess the same material properties as Grade 36 steel, actually they were different in terms of mechanical properties and chemical compositions according to the mill test certificates provided by the steel companies. These crucial parameters are listed in Table 6.1.

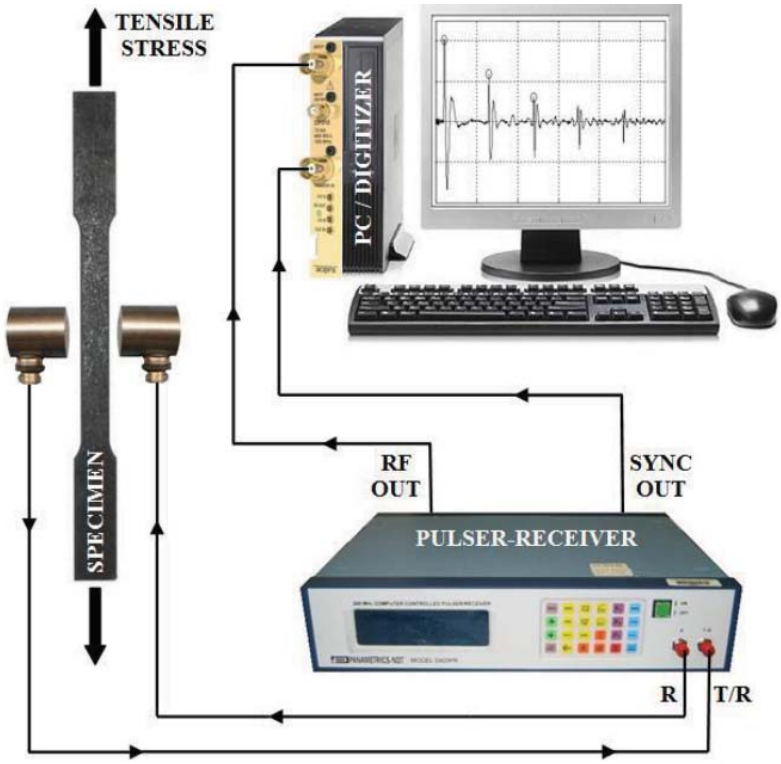

Figure 6.1: The experimental setup and the assembly of the main units.

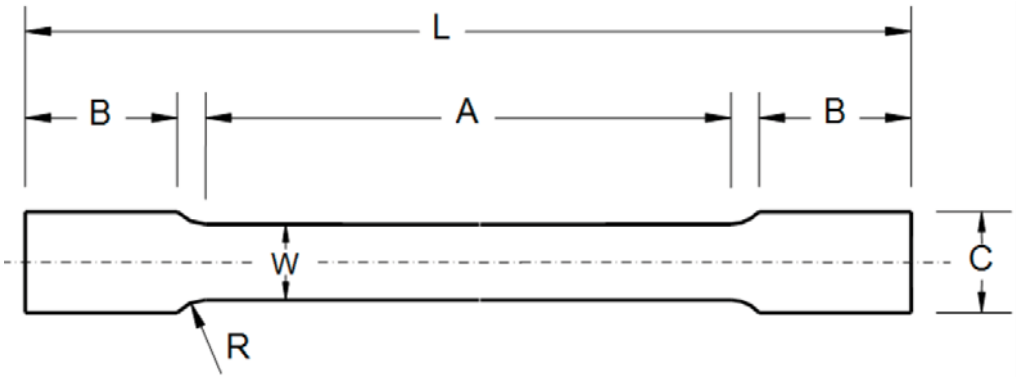

	Dimension (in)
W - Width	0.5
R - Radius of fillet	0.5
L - Overall length	8
A - Length of reduced section	3.35
B - Length of grip section	2
C - Width of grip section	0.75

Figure 6.2: Dimensions of the dog-bone shaped specimens.

Table 6.1: The Specimen Material Properties based on Mill Test Certificates

Specimen Type	Specimen Thickness	Average Mechanical Properties		Chemical Decomposition				
		Tensile Stress	Yield Stress	C (carbon)	Si (silicon)	Mn (manganese)	P (phosphorus)	S (sulfur)
	(in)	(ksi)	(ksi)	$\times$ 100			$\times$ 1000	
Type I	1/4	63.1	46.3	9	20	68	17	9
Type II	3/8	61.7	50.7	6	19	72	14	5
Type III	1/4	65.3	43.5	16	6	88	15	24
Type IV	1/8	63.3	46.9	13	1.5	37	13	10

The ultrasonic testing system was built to test the specimens with the above-mentioned material properties. In addition, ultrasonic measurements were taken at the targeted stress levels by piezoelectric longitudinal and shear wave transducers using the through transmission and pulse-echo test-modes. The first step of this experiment was cleaning the surfaces of the specimens where the transducers were going to be placed and sanding the specimens to improve the contact between the transducers and the specimens. Secondly, different force values were entered to the Model 793.10 multipurpose testware software to control the MTS 810 testing system (see Fig. 6.3). This system depicted in Fig. 6.3 was used to apply the desired levels of uniaxial tensile stresses to the test specimens at which ultrasonic measurements were aimed to be taken. All test specimens were subjected to forces corresponding to a stress resolution of 10 ksi in the elastic range of the materials, while for stress levels close to and beyond yielding, higher stress-resolution values were applied between 2.5 and 5 ksi. Totally, twenty-eight groups of ultrasonic tests were conducted on these steel specimens, where the specimens were loaded up until failure at the targeted stress levels before and after yielding. Note that in fifteen groups among these tests, ultrasonic signals propagated through the midsection of the specimens, while the top, middle, and bottom sections were propagated through by ultrasound for the remaining thirteen groups. Besides, in all the ultrasonic tests, the transducers were placed so that the signals could propagate through the specimens in a direction perpendicular to the loading. Therefore, five hundred and eighty-two ultrasonic signal sequences were collected accordingly. Finally, we performed the automatic yield detection method summarized in Section 5 for all these signals via computer simulations.

Simulation results are presented here to demonstrate the performance of the proposed auto-

Figure 6.3: MTS 810 hydraulic materials testing system.

matic yield detection scheme. E_1 is the energy for the first frame of ultrasonic signal and E_{k_p} is the *maximum frame energy* (see [13] for details). The threshold parameters are chosen as follows: $\kappa_{th} = 0.01$, $\epsilon_{th} = 0.1E_{k_p} + 0.9E_1$, $\zeta_{th}^{\mathrm{B}} = 0.2$, $\delta n_{\max}^{\mathrm{B}} = (\hat{q}_1 - \hat{p}_1/6)$, $\zeta_{th}^{\mathrm{W}} = 0.1$, $\delta n_{\max}^{\mathrm{W}} = (\tilde{q}_1 - \tilde{p}_1/6)$, $\rho_{th} = 10$, $\mathcal{SNR}_{th} = 15,\ 20,\ 25,\ 30$ dB, respectively, where $\tilde{p}_1$ and $\tilde{q}_1$ are the starting and terminal points of the subwavelet template $h_{a,b}(n)$. Please refer to [13] for further clarification. A typical example of ultrasonic signal can be visualized in Fig. 4.1. First, we would like to compare the proposed BSSEM method with the prevalent wavelet-based peak detection method. According to the discussion in Section 3.2, the wavelet-based peak detection method would perform well only if the mother wavelet is chosen appropriately.

In other words, the mother wavelet should resemble the signal signature. Thus, we have tested a variety of mother wavelets from different wavelet families and have found that in the Biorthogonal wavelet family [35], the wavelet function $\Psi(n)$ of bior1.5 (see [36]) leads to the best performance in terms of the highest peak detection rate. This mother wavelet function $\Psi(n)$ is depicted in Fig. 6.4. The comparative study of these two peak detection methods can be reflected by the ROC curve in Fig. 6.5, which results from the entire ultrasonic signal data set as previously stated. It is obvious that our proposed BSSEM greatly outperforms the wavelet-based method. The detection performance (correct detection rate) margin is around 5% across almost all false detection rates. Thus, we choose the BSSEM method to identify the peak locations of the ultrasonic echoes due to its superiority.

After the peak locations are identified, we carry out Algorithm 1 and the SNR threshold to determine the starting and terminal time points of the effective echoes in the ultrasound. Then we can extract the average energy E for each ultrasonic signal. Note that the average energy E needs to be "normalized" with respect to the average energy of the same specimen at zero stress level. Then the normalized average energy of the ultrasonic signal is compared to the optimal classification threshold which results from the training data according to the procedure stated in [16]. Then, the appropriate stress state (before or after yield) for the testing specimen can be determined. To determine the optimal classification threshold, ROC analysis is employed according to [16]. The threshold is gradually changed from zero to the maximum average energy among all training data. Thus, the measures $\mathcal{CDR}$, $\mathcal{FDR}$, and $\mathcal{AUC}$ can be obtained for each threshold. Table 6.2 lists these measures for different thresholds. For example, if we restrict $\mathcal{FDR} \leq 20\%$ and $\mathcal{CDR} \geq 94\%$, then the optimal classification threshold $\vartheta_{th} = 1$ should be selected.

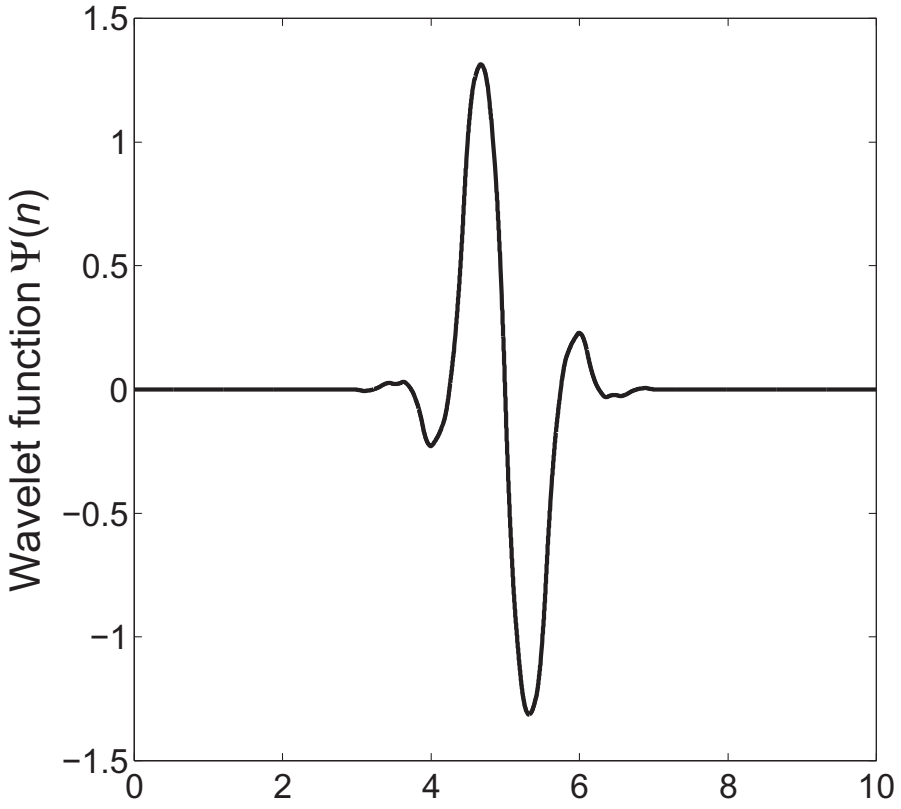

Figure 6.4: Biorthogonal wavelet: bior1.5.

After the measures of $\mathcal{CDR}$ and $\mathcal{FDR}$ are obtained, we may establish the ROC curves. We vary the SNR threshold ($\mathcal{SNR}_{th}$=15, 20, 25, and 30 dB) to collect different numbers of effective echoes for dynamically extracting the average energy features. Thus, different ROC curves can be engendered with respect to different $\mathcal{SNR}_{th}$ values. On the other hand, we also choose the first echo only ($m^* = 1$) so as to establish another ROC curve. Finally, we generate the ROC curve using the average energy features resulting from the effective echoes subject to $\mathcal{SNR}_{th}$=30 dB, where all the starting and terminal time points are marked manually (they can be considered as the ground truth). The results from the entire database are depicted in Fig. 6.6. According to Fig. 6.6, one can discover that the yield detector

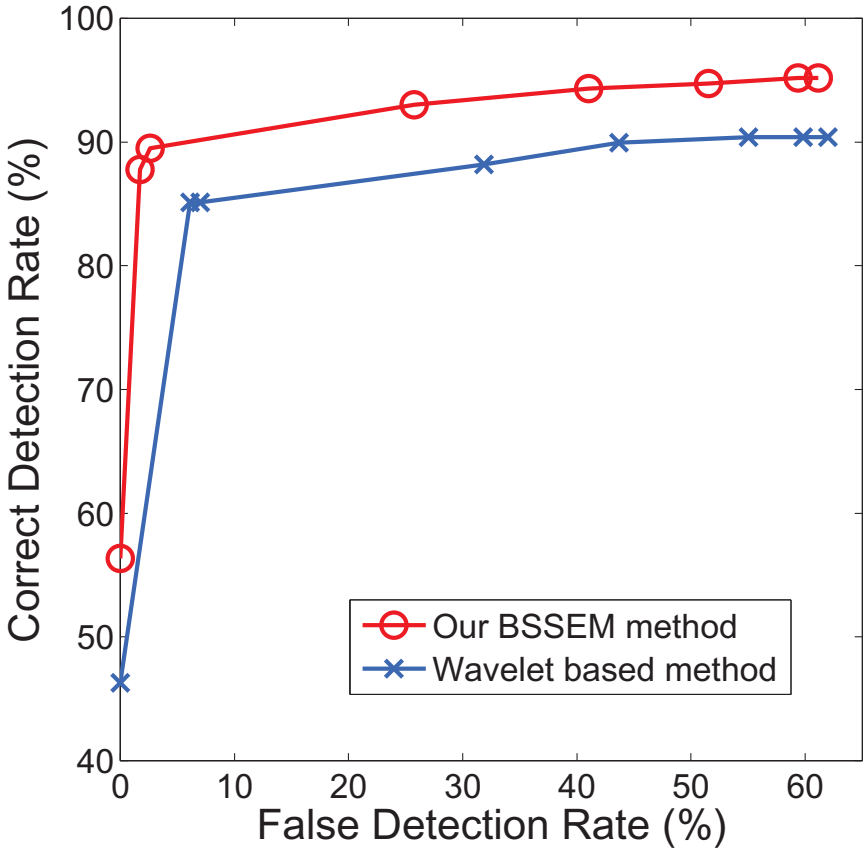

Figure 6.5: Receiver-operating-characteristic curves for comparison of multi-ridge detection schemes.

based on the "ground truth" (labeled as "Manual operation" in the figure) leads to the best detection performance. For the yield detector based on the dynamical echo selection subject to different SNR thresholds, the larger SNR threshold, the better detection performance can be obtained. Moreover, the detector based on the "best" echo (the first echo) is outperformed by the detector based on the dynamical echo selection with $\mathcal{SNR}_{th}$=30 dB. Consequently, the new proposed novel automatic yield detection scheme can reach very close to the optimal detection performance but save a lot of human efforts. Hence, the new proposed technique is very practical and useful for the future ultrasonic NDT instrumentation.

Table 6.2: $\mathcal{CDR}$, $\mathcal{FDR}$, and $\mathcal{AUC}$ Measures for ROC Analysis

Threshold	$\mathcal{CDR}$	$\mathcal{FDR}$	Threshold	$\mathcal{CDR}$	$\mathcal{FDR}$
0.00	0.0000	0.0000	1.10	0.9820	0.3704
0.10	0.2973	0.0000	1.20	1.0000	0.5802
0.20	0.6486	0.0000	1.30	1.0000	0.8025
0.30	0.7748	0.0000	1.40	1.0000	0.8889
0.40	0.8018	0.0000	1.50	1.0000	0.9259
0.50	0.8378	0.0000	1.60	1.0000	0.9753
0.60	0.8468	0.0000	1.70	1.0000	0.9753
0.70	0.8739	0.0000	1.80	1.0000	0.9877
0.80	0.9189	0.0000	1.90	1.0000	1.0000
0.90	0.9369	0.0247	2.00	1.0000	1.0000
1.00	0.9459	0.1852			
$\mathcal{AUC} = 0.9803$					

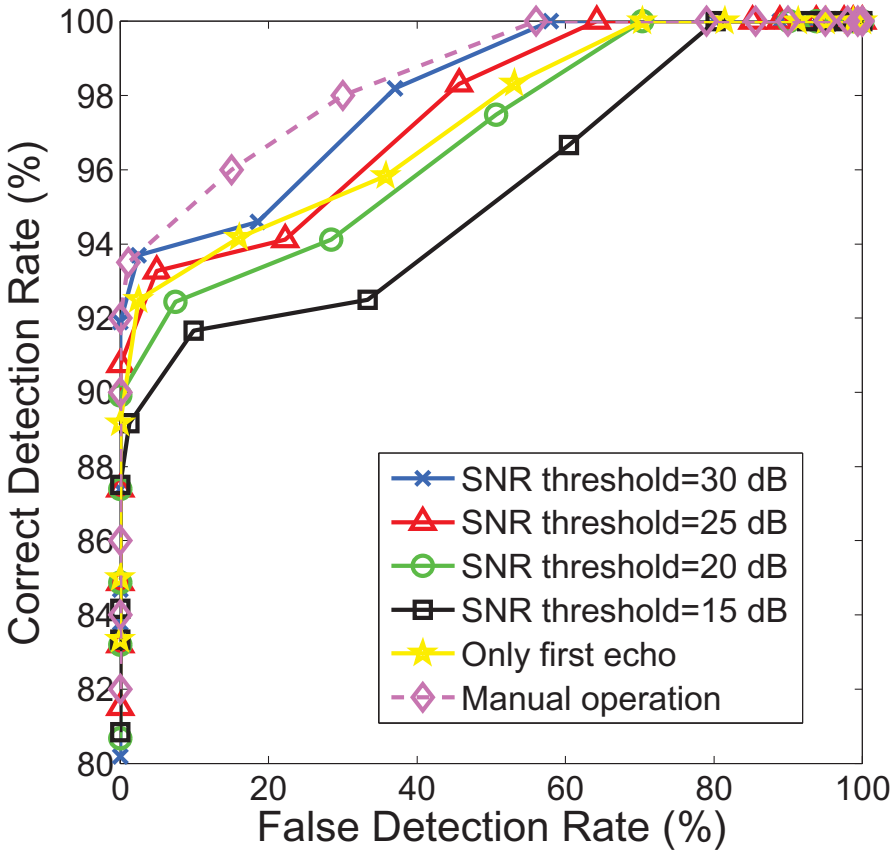

Figure 6.6: Receiver-operating-characteristic curves for different kinds of yield-detection schemes.

7. CONCLUSION

In this thesis, we compare the previously proposed blind-signature-signal-extraction based multiridge-detection (BSSEM) method with the wavelet-based peak detection scheme. It is found that the former detection method is superior to the latter scheme. Based on the BSSEM technique, we design a novel automatic yield detection technology, which can blindly and dynamically extract effective echoes based on a preset signal-to-noise ratio threshold. Then the normalized average energy over the effective echoes can be used for the yield detection in steel structures. The receiver-operating-characteristic curves resulting from the collected large database demonstrate that the novel proposed automatic yield detection scheme can approach the optimal detection performance (resulting from the manual operation) while the manual operation is not necessary thereupon. This proposed new scheme would be very beneficial to the future development of easy-to-use yield-detection nondestructive testing (NDT) tools.

BIBLIOGRAPHY

[1] A. J. Hunter, B. W. Drinkwater, and P. D. Wilcox, "Least-squares estimation of imaging parameters for an ultrasonic array using known geometric image features," *IEEE Transactions on Ultrasonics, Ferroelectrics, and Frequency Control*, vol. 58, pp. 414–426, Feb. 2011.

[2] J. yu Lu, H. Zhou, and J. F. Greenleaf, "Biomedical ultrasound beamforming," *Ultrasound in Medicine and Biology*, vol. 20, pp. 403–428, July 1994.

[3] S. Alzebda and A. N. Kalashnikov, "Ultrasonic sensing of temperature of liquids using inexpensive narrowband piezoelectric transducers," *IEEE Transactions on Ultrasonics, Ferroelectrics, and Frequency Control*, vol. 57, pp. 2704–2711, Dec. 2010.

[4] H. Sohn and S. B. Kim, "Development of dual PZT transducers for reference-free crack detection in thin plate structures," *IEEE Transactions on Ultrasonics, Ferroelectrics, and Frequency Control*, vol. 57, pp. 229–240, Jan. 2010.

[5] J. Yang and I. C. Ume, "Laser ultrasonic technique for evaluating solder bump defects in flip chip packages using modal and signal analysis methods," *IEEE Transactions on Ultrasonics, Ferroelectrics, and Frequency Control*, vol. 57, pp. 920–932, Apr. 2010.

[6] Z. You, M. Lusk, R. Ludwig, and W. Lord, "Numerical simulation of ultrasonic wave propagation in anisotropic and attenuative solid materials," *IEEE Transactions on Ultrasonics, Ferroelectrics, and Frequency Control*, vol. 38, pp. 436–445, Sept. 1991.

[7] E. C. Johnson, J. D. Pollchik, and J. N. Schurr, "An ultrasonic testing technique for measurement of the poisson's ratio of thin adhesive layers," *Review of Progress in Quantitative Nondestructive Evaluation*, vol. 11, pp. 1291–1298, July 1992.

[8] G. G. Leisk and A. Saigal, "Digital computer algorithms to calculate ultrasonic wave speed," *Material Evaluation*, vol. 54, pp. 840–843, July 1996.

[9] A. P. Mouritz, "Ultrasonic and interlaminar properties of highly porous composites," *Journal of Composite Material*, vol. 34, pp. 218–239, Feb. 2000.

[10] K. J. Newell, A. N. Sinclair, Y. Fan, and C. Georgescu, "Ultrasonic determination of stiffness properties of an orthotropic viscoelastic material," *Research Nondestructive Evaluation*, vol. 9, no. 1, pp. 25–39, 1997.

[11] C. S. Karthikeyan, C. R. L.Murthy, S. Sankaran, and Kishore, "Characterization of reinforced syntactic foams using ultrasonic imaging techniques," *Bulletin of Material Science*, vol. 22, pp. 811–815, June 1999.

[12] N. Gupta and E. Woldesenbet, "Hygrothermal studies on syntactic foams and compressive strength determination," *Composite Structures*, vol. 61, pp. 311–320, Sept. 2003.

[13] H.-C. Wu, N. Gupta, and P. S. Mylavarapu, "Blind multiridge detection for automatic nondestructive testing using ultrasonic signals," *IEEE Transactions on Ultrasonics, Ferroelectrics, and Frequency Control*, vol. 53, pp. 1902–1911, Oct. 2006.

[14] R. A. Carmona, W. L. Hwang, and B. Torresani, "Multiridge detection and time-frequency reconstruction," *IEEE Transactions on Signal Processing*, vol. 47, pp. 480–492, Feb. 1999.

[15] R. A. Carmona, W. L. Hwang, and B. Torresani, "Characterization of signals by the ridges of their wavelet transforms," *IEEE Transactions on Signal Processing*, vol. 45, pp. 2586–2590, Oct. 1997.

[16] Y. Bingol, *Development of an ultrasonic NDE&T tool for yeild detection in steel structures*. PhD thesis, Louisiana State University, Aug. 2008.

[17] A. M. Sabatini, "A digital-signal-processing technique for ultrasonic signal modeling and classification," *IEEE Transactions on Instrumentation and Measurement*, vol. 50, pp. 15–21, Aug. 2002.

[18] H. L. V. Trees, *Detection, estimation and modulation theory*. New York: Wiley, 2001.

[19] A. M. Mood, F. A. Graybill, and D. C. Boes, *Introduction to the Theory of Statistics*. Boston: McGraw-Hill, 3 ed., 1974.

[20] A. Abbate, J. Koay, J. Frankel, S. C. Schroeder, and P. Das, "Application of wavelet transform siganl processor to ultrasound," in *Proceedings of IEEE Ultrasonics Symposium*, pp. 1147–1152, Nov. 1994.

[21] S. Kim, J. McNames, and K. Burchiel, "Action potential detection with automatic template matching," in *Proceedings of 26th Annual International Conference of the IEEE Engineering in Medicine and Biology Society*, vol. 1, pp. 41–44, Sept. 2004.

[22] K. Vijayalakshmi and A. M. Abhishek, "Spike detection in epileptic patients EEG data using template matching technique," *International Journal of Computer Applications*, vol. 2, pp. 5–8, June 2010.

[23] S. Kim and J. McNames, "Automatic spike detection based on adaptive template matching for extracellular neural recordings," *Journal of Neuroscience Methods*, vol. 165, pp. 165–174, Sept. 2007.

[24] A. B. Doser and M. E. Dunham, "Transionospheric signal detection with chirped wavelets," in *Conference Record of the Thirty-First Asilomar Conference on Signals, Systems & Computers*, vol. 2, pp. 165–174, Nov. 1997.

[25] E. Oruklu and J. Saniie, "Ultrasonic flaw detection using discrete wavelet transform for nde applications," in *Proceedings of IEEE Ultrasonics Symposium*, vol. 2, pp. 1054–1057, Aug. 2004.

[26] T. Celik and K.-K. Ma, "Multitemporal image change detection using undecimated discrete wavelet transform and active contours," *IEEE Transactions on Geoscience and Remote Sensing*, vol. 49, pp. 706–716, Feb. 2011.

[27] A. S. Zandi, M. Javidan, G. A. Dumont, and R. Tafreshi, "Automated real-time epileptic seizure detection in scalp EEG recordings using an algorithm based on wavelet packet transform," *IEEE Transactions on Biomedical Engineering*, vol. 57, pp. 1639–1651, July 2010.

[28] M. A. S. Masoum, S. Jamali, and N. Ghaffarzadeh, "Detection and classification of power quality disturbances using discrete wavelet transform and wavelet networks," *IET Science, Measurement & Technology*, vol. 4, pp. 193–205, July 2010.

[29] T. Fawcett, "An introduction to ROC analysis," *Pattern Recognition Letters*, vol. 27, pp. 861–874, June 2006.

[30] D. J. Vining and G. W. Gladish, "Receiver operating characteristic curves: a basic understanding," *Radio Graphics*, vol. 12, pp. 1147–1154, Nov. 1992.

[31] P. Kolan, R. Vaithilingam, and R. Dantu, "Automatic calibration using receiver operating characteristics curves," in *Proceedings of the 2007 2nd International Conference on Communication System Software and Middleware and Workshops*, vol. 10, (COMSWARE 2007, Institute of Electrical and Electronics Engineers Computer Society, Piscataway, NJ 08855-1331, United States), pp. 1–8, Jan. 2007.

[32] C. Marzban, "The ROC curve and the area under it as performance measures," *Weather and Forecasting*, vol. 19, pp. 1106–1114, June 2004.

[33] A. P. Bradley, "Use of the area under the ROC curve in the evaluation of machine learning algorithms," *Pattern Recognition*, vol. 30, pp. 1145–1159, July 1997.

[34] ASTM, *ASTM E8-04 standard test methods for tension testing of metallic materials*, 2004.

[35] A. Cohen, I. Daubechies, and J. C. Feauveau, "Biorthogonal bases of compactly supported wavelets," *Communications on Pure and Applied Mathematics*, vol. 45, pp. 485–560, June 1992.

[36] M. Misiti, Y. Misiti, G. Oppenheim, and J.-M. Poggi, *Wavelet toolbox user's guide*. Mathworks Inc., 2011.

VITA

Hongting Zhang received a bachelor electrical engineering degree from Harbin Institute of Technology, in 2009. She is currently pursuing the degree of Doctor of Philosophy in the department of Electrical and Computer Engineering, Louisiana State University, Baton Rouge. Her research interests are in the areas of wireless communications and statistical signal processing.